Architecture-process relationships in stochastic honeycombs

Megan Hostetter, Glenn Hibbard

Department of Materials Science and Engineering, University of Toronto, Toronto, Ontario, Canada M5S 3E4
Correspondence to: G. Hibbard (E-mail: glenn.hibbard@utoronto.ca)

ABSTRACT: Stochastic honeycomb sandwich panels are fabricated through a simple process of melt-stretching molten polymer blanks. This study mapped their internal architecture over a wide domain of material process space, defined by the areal density and melt-stretch rate. The internal architectures were characterized using both topological and geometric parameters: the node density, the total length of webs, the Euler number, and a characteristic fractal area fraction. The mechanical response of the polymer melt was quantified in terms of peak stress and stiffness, along with apparent elongation viscosity. The observed architectures and polymer melt responses were consistent with a varying activated entanglement density in the melt and illustrate how the fabrication conditions can be tuned to obtain a desired architecture. © 2015 Wiley Periodicals, Inc. J. Appl. Polym. Sci. **2015**, *132*, 42174.

INTRODUCTION

Cellular plastics have become increasingly important for high-strength low-weight applications over the last few decades,[1] with more recent attention being turned to fully recyclable products.[2,3] Polypropylene (PP) stochastic honeycombs have been shown to have similar mechanical properties to conventional PP honeycombs and superior mechanical properties to PP foams.[4] They are fabricated by melting PP between Al platens and then uniaxially stretching the polymer melt to a specified height. Complete sandwich panels can be fabricated out of a single material without blowing agents or adhesives, making them fully recyclable.[4] After cooling, the structure consists of two as-fabricated face sheets, or skins, separated by a network of interconnected webs. While stochastic honeycombs have a random internal structure, they nevertheless exhibit repeatable, predictable mechanical properties.[4,5]

Previous work has examined how the internal architecture changes with properties of the polymer melt, such as the melt flow index (MFI) and the zero-shear viscosity (η_o).[6] The presence of long-chain branches increases the entanglement density with branches acting as entanglement points with primary bonds as opposed to secondary bonds; branched PPs formed stochastic honeycombs with many more webs and web branch nodes than linear PP,[6] implying a greater number of activated entanglement points. The melt flow properties of PP were thus previously shown to affect the architecture of stochastic honeycombs. For the first time, this study looks at using the mechanical response of the polymer melt during melt stretching as a means to characterize differences in web interconnectivity (and thus of activated entanglements).

EXPERIMENTAL

PP sheets were fabricated by melting PP beads (MFI = 2.4 g/10 min, ASTM D1238[7]) at $1.1 T_m$ (180°C) between Al platens attached to a Shimadzu AG-N UTM. The temperature was controlled using a Shimadzu TCE-N300 Thermostatic Chamber. A force of 500 N was applied to the PP melt, and the stroke was held constant as the PP sheet cooled in air. Disc-shaped blanks of PP were cut from the sheets (thickness, t_{blank} = 1.5–4.5 mm and diameter, d_{blank} = 8.2 ± 0.3 cm) with areal densities ($\rho_{A,blank}$) ranging from 0.13 to 0.37 g/cm². Stochastic honeycombs were fabricated from the blanks (again at $1.1 T_m$), by applying a preliminary compressive force (F_{app} = 200–5000 N) at 10 mm/min, before melt stretching at varying elongation rates of $\dot{S}$ = 1, 10, 30, 60, and 100 mm/min (corresponding to strain rates of $\dot{\varepsilon} \approx$ 0.005, 0.040, 0.125, 0.235, and 0.370 s^{-1}) in ambient air to a height of 10 mm. The temperature of the platens was monitored using a thermocouple with leads attached at opposing corners. Five samples were fabricated in each set of conditions, and were then illuminated from underneath and photographed. The photographs were edited in ImageJ to produce binary images of the two-dimensional projection of the webs that could be used as inputs for analysis in ImageJ and MatLab.
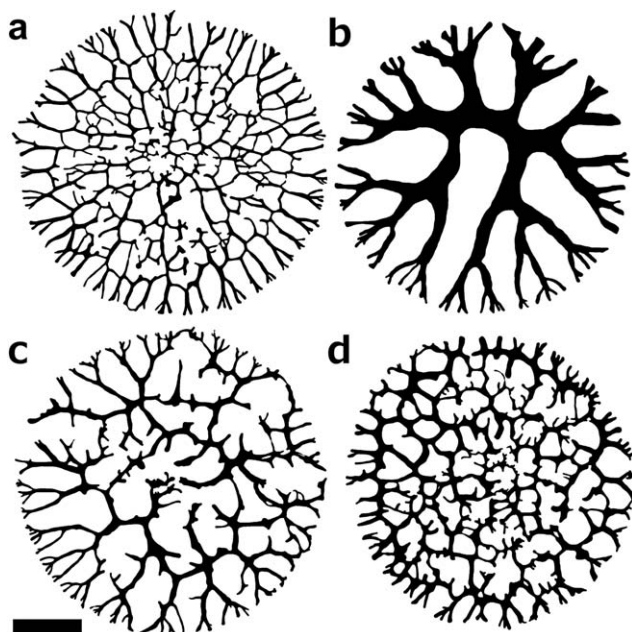
Figure 1. Examples of the widely different architectures formed over the fabrication space considered, with elongation rate $\dot{S} = 10$ mm/min and areal density $\rho_A = 0.09$ g/cm^2 (a) and $\rho_A = 0.23$ g/cm^2 (b), and $\rho_A = 0.15$ g/cm^2 and $\dot{S} = 1$ mm/min (c), and 100 mm/min (d). Scale bar indicates a length of 20 mm.
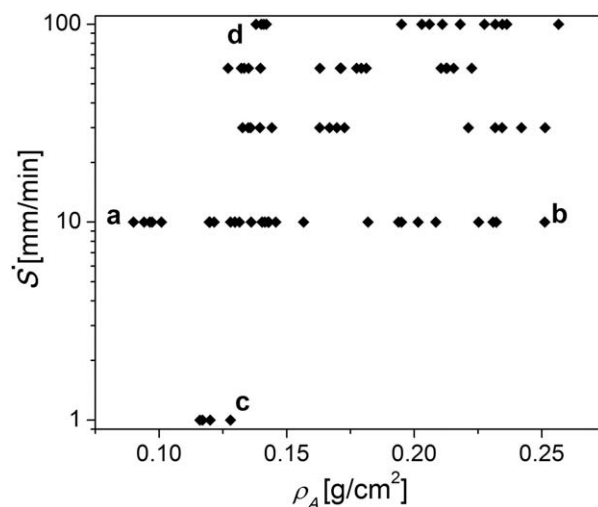

Figure 2. Process Map illustrating the range of fabrication space (elongation rate, $\dot{S}$, and areal density, ρ_A) considered. The points labelled a–d correspond to the two-dimensional projections seen in Figure 1.

RESULTS AND DISCUSSION

Architecture

While the process to fabricate stochastic honeycombs is simple, their internal architecture is not. Previous work analyzed the three-dimensional architecture of stochastic honeycombs through X-ray tomography using area fractions and Minkowski functionals (surface area, volume, and Euler number).[5,6] The cross-sectional area fraction (area of the skin or webs/area of the sample) was shown to decrease from 1 at the upper and lower skins to a plateau over the central third of the sample height, which varied with the relative density of the sample.[6] Surface area and volume, two of the Minkowski functionals in three-dimensions, were combined into an internal surface area to volume ratio, which was found to decrease as the core density increased, and could be used to obtain a value for the effective web thickness.[5] In contrast, this study focuses on the formation of the initial web pattern; the simple back-lit images given in Figure 1 are able to illustrate this formation, and are used as the basis of architectural characterization. Due to the presence of internal archways and partial webs, the projection of the webs on either side of the samples varied slightly as only the webs directly in contact with the skin were imaged, but the variation within one sample was inside the standard deviation of the samples fabricated under identical conditions.

Figure 2 presents a process map of the elongation rates, $\dot{S}$, and areal densities, ρ_A, used during melt stretching. The areal densities varied by a factor of three and the melt-stretch rate by two orders of magnitude. Figure 3 shows the webs of samples fabricated with $\dot{S} = 10$ mm/min and ρ_A over the range of 0.10 g/cm^2 to 0.23 g/cm^2. Over this density range, the structure

changes dramatically. At $\rho_A = 0.10$ g/cm^2 the structure has a large number of branch points, or nodes, and a large total length of webs. As ρ_A increases, the number of nodes, N, decreases and the total length of webs, L, decreases as well. Figure 4 shows the webs of five samples at constant areal density ($\rho_A = 0.13$ g/cm^2) and with the melt stretch rate changing from $\dot{S} = 1$ mm/min to 100 mm/min. Qualitatively, the distance between nodes becomes smaller and the number of nodes increases as $\dot{S}$ increases. N and L are plotted as a function of ρ_A for $\dot{S} = 10$ mm/min and 100 mm/min in Figure 5. N and L both decrease as ρ_A increases, and increase as $\dot{S}$ increases. Both variables depend more strongly on ρ_A than $\dot{S}$, and there appears to be a larger difference between $\dot{S} = 10$ mm/min and $\dot{S} = 100$ mm/min at low densities for N. A greater number of nodes implies a more branched structure and a greater number of connecting webs. Figure 6 plots N against L for $\dot{S} = 10$ mm/min and 100 mm/min; for each $\dot{S}$, the samples fit along a linear line, in which ρ_A decreases as N and L increase. As $\dot{S}$ decreases from 100 mm/min to 10 mm/min, the slope of the N–L plot decreases from 4.3 nodes/cm to 2.4 nodes/cm. N/L can be calculated for each sample, and this value is in effect the number of nodes per unit length of web.

Two samples with $N/L = 1.18$ cm^{-1} ($\rho_A = 0.21$ g/cm^2, $\dot{S} = 10$ and 100 mm/min) are shown in Figure 7. In the two-dimensional projection, the sample at lower $\dot{S}$ [Figure 7(a)] has a more open structure, while the sample at higher $\dot{S}$ [Figure 7(b)] has more (projected) closed cells. This can be seen through the Euler number (χ) which is a measure used in two-dimensional cellular solids and 3D foams to give a quantitative value for the connectedness of a structure.[1,8] Practically, χ is determined through image analysis by subtracting the number of "holes" in an area (shaded in Figure 7) from the number of connected areas.[9,10] Note that over the entire three-dimensional structure of the stochastic honeycombs, $\chi_{3D} = 1$, since each pore must be connected back to the sample perimeter. In a two-dimensional projection, however, partial webs give the appearance of closed cells, which relates to the tortuosity of the path
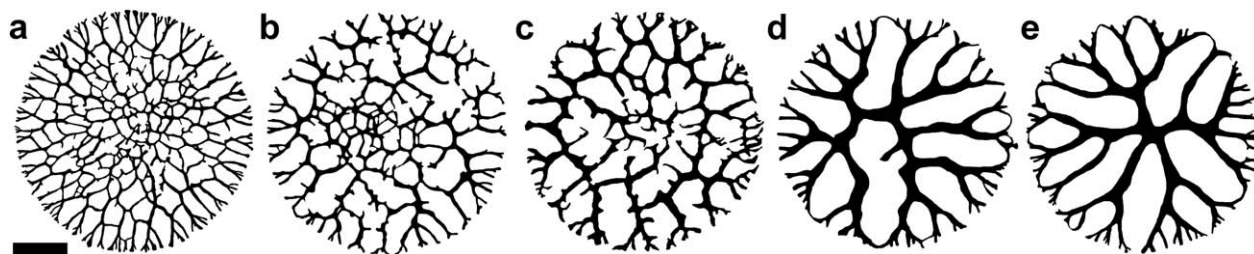
Figure 3. The two-dimensional projections of the webs for five samples fabricated at $\dot{S} = 10$ mm/min and with $\rho_A = 0.10$ g/cm^2 (a), 0.13 g/cm^2 (b), 0.16 g/cm^2 (c), 0.19 g/cm^2 (d), and 0.23 g/cm^2 (e). Scale bar indicates a length of 20 mm.

from sample perimeter to centre. For the samples in Figure 7, the values of χ are -5 and -25, respectively; Figure 7(b) has a more connected structure with a greater number of 'closed' cells (i.e., partial webs) than Figure 7(a). Over the entire range of samples, χ ranged from 0 ($\rho_A = 0.23$ g/cm^2, $\dot{S} = 10$ mm/min) to -94 ($\rho_A = 0.14$ g/cm^2, $\dot{S} = 100$ mm/min).

The connectedness of the structure can also be quantified by examining the area fraction of the (apparently) closed cells. At the outer perimeter there is a fractal-like structure that extends some (varying) distance towards the centre of the sample before the webs become interconnected. This length scale is expressed as an area fraction of the sample in which the webs are not interconnected, and is calculated through 1 minus the area fraction of closed cells, disregarding the area of the webs:

$$\lambda = 1 - A_{\text{cells}} / (A_{\text{total}} - A_{\text{webs}}) \tag{1}$$

where A_{cells} is the area of the closed cells, A_{total} is the area of the stochastic honeycomb sample, A_{webs} is the area of the webs, and λ is the fractal area fraction. λ represents the outer area fraction of air ingress through which the fractal nature of the stochastic honeycomb extends. For the image in Figure 7(a), $\lambda = 0.75$, while for Figure 7(b), $\lambda = 0.48$. In general χ and λ are negatively correlated.

Overall, N/L, χ, and λ all change with the areal density and with the melt stretch rate. To illustrate how the architecture varies over the range of samples fabricated, contour lines representing the ratio N/L was superimposed on the Process Map, where the samples are grouped by their values of χ (Figure 8). The values of N/L increase as ρ_A decreases and $\dot{S}$ increases, and the same is generally true for χ.

Fabrication

In order to understand how these internal architectures form, one would like to have an *in situ* process parameter that can be

used to track the state of the system during fabrication. The force required to maintain the fixed melt stretching rate as a function of displacement is a useful indicator because it provides a value for the overall response of the molecular chains. Figure 9 presents the force response (normalized by the area of the melt-compressed blank to give an effective stress) over one complete fabrication cycle ($\dot{S} = 10$ mm/min and $\rho_A = 0.21$ g/cm^2), where tension is defined to be positive. This process can be considered as having four stages. In Stage I, the molten blank is compressed to a preselected force at a compression rate of 10 mm/min. The melt flows outward on the platens as t_{blank} decreases to t_{melt} and d_{blank} increases to d_{final}. In Stage II, the compressive load is removed and melt is stretched uniaxially in air at a selected elongation rate between 1 and 100 mm/min. Initially, the polymer experiences elastic recovery, but once $\sigma > 0$ it is under tension at a constant melt stiffness (E_{melt}) and the stress increases to a peak tensile stress. Stage III begins at the peak stress (σ_{pk}) with the creation of new internal surface area due to a combination of flow of the polymer chains and air infiltration. Air ingress then inflates the core, creating the webs of the stochastic honeycomb, and the stress decreases quickly. In Stage IV, the stress reaches a nearly constant value as the final web pattern has been formed and the webs stretch at the plateau extensional value (σ_{ext}). Some of the webs undergo ductile failure as the sample is stretched to its final height, t_{final}, and partial webs and archways are formed.[6] Note that previous work showed that there was some small increase in the crystallinity of the PP in the webs compared to the PP with no thermal history, implying that some strain-induced crystallinity occurs as a result of melt stretching.[6] The temperature at each stage as a function of the elongation rate is detailed in Table I.

Figure 10 shows the tensile portion of the fabrication curves for four samples. Figure 10(a) compares samples fabricated with $\dot{S} = 10$ mm/min at $\rho_A = 0.09$ and 0.23 g/cm^2. The lower density
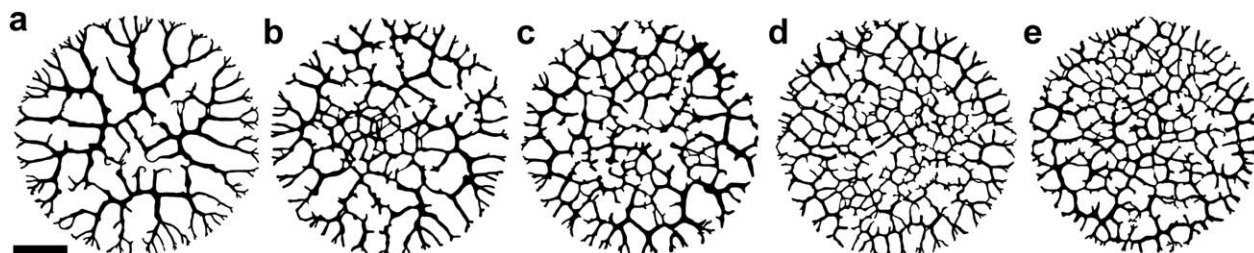

Figure 4. The two-dimensional projections of the webs for five samples fabricated with $\rho_A = 0.13$ g/cm^2 and $\dot{S} = 1$ mm/min (a), 10 mm/min (b), 30 mm/min (c), 60 mm/min (d), and 100 mm/min (e). Scale bar indicates a length of 20 mm.
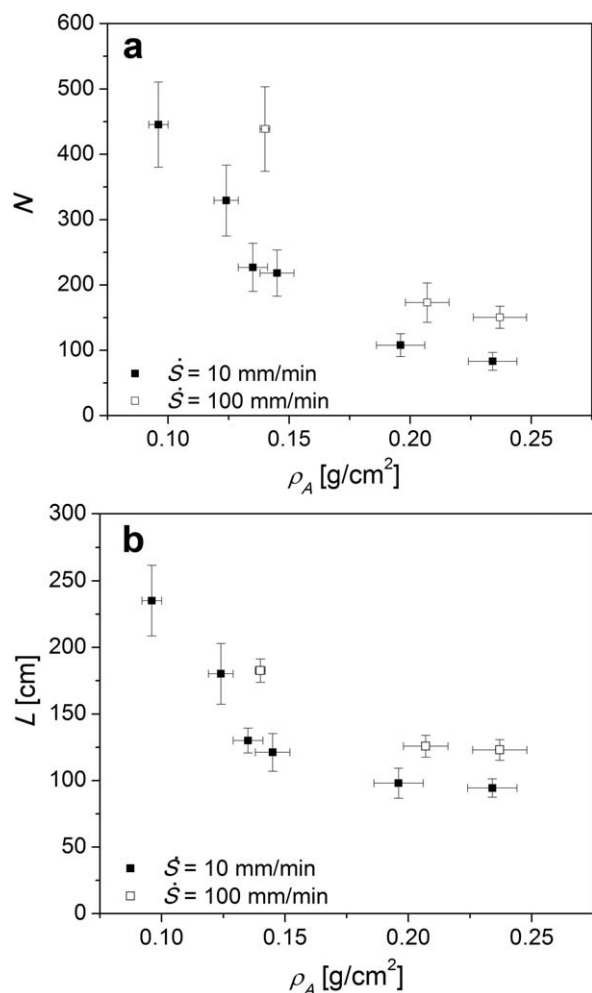
Figure 5. The number of nodes, N (a), and the total length of webs, L (b), plotted against ρ_A for $\dot{S} = 10$ mm/min and 100 mm/min.

Figure 7. Two-dimensional projections for samples having the same areal density and N/L values ($\rho_A = 0.21$ g/cm^2 and $N/L = 1.18$ cm^{-1}) but with $\chi = -5$ (a) and -25 (b). These samples were fabricated at $\dot{S} = 10$ mm/min and $\dot{S} = 100$ mm/min respectively. Scale bar indicates a length of 20 mm.

E_{melt}, and a larger σ_{ext}. Figure 11 plots σ_{pk} as a function of ρ_A for $\dot{S} = 10$ and 100 mm/min. σ_{pk} decreases as a function of density for $\dot{S} = 10$ mm/min, but as $\dot{S}$ increases, σ_{pk} becomes less dependent on ρ_A, and is independent of ρ_A by $\dot{S} = 100$/min. σ_{pk}, E_{melt} and σ_{ext} are plotted as a function of $\dot{\varepsilon}$ for $\rho_A = 0.13$ g/cm^2 in Figure 12. σ_{pk}, E_{melt}, and σ_{ext} all increase as $\dot{\varepsilon}$ increases, independent of density.

It is well known that the tensile strength and stiffness of polymers below their crystallization temperature are strain-rate dependent;[11,12] this is also true for polymer melts,[13–15] although the strength and stiffness are not often measured. At the beginning of the melt extension (Stage II), the polymer is relaxing while the net compressive stress is being reduced. An additional set of tests were conducted where the samples were held at the compressed thickness for 15 s before extension began (i.e. loading to a preset force and then holding at that displacement). From these tests, an effective relaxation rate of $\tau_{relax} = 2.1 \pm 0.1$ kPa/s was determined from the stress-time curve. This value

sample has a higher σ_{pk} and a larger E_{melt}, while σ_{ext} does not vary with density. Figure 10(b) compares two samples with $\rho_A = 0.14$ g/cm^2 and $\dot{S} = 1$ mm/min and 100 mm/min. The sample with the higher elongation rate has a larger σ_{pk}, a higher
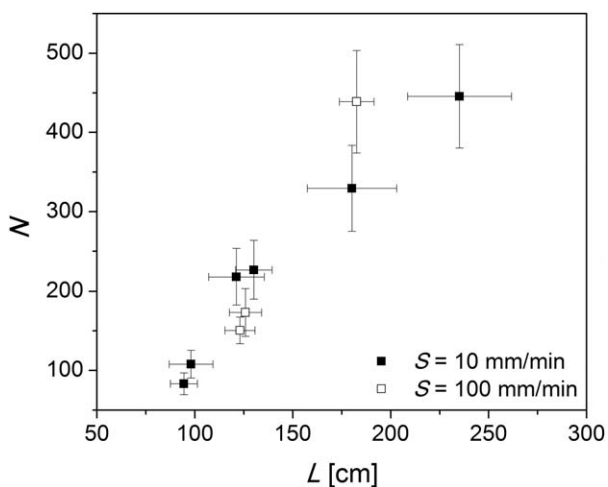

Figure 6. The number of nodes, N, plotted against the total web length, L for melt stretch rates of 10 mm/min and 100 mm/min.
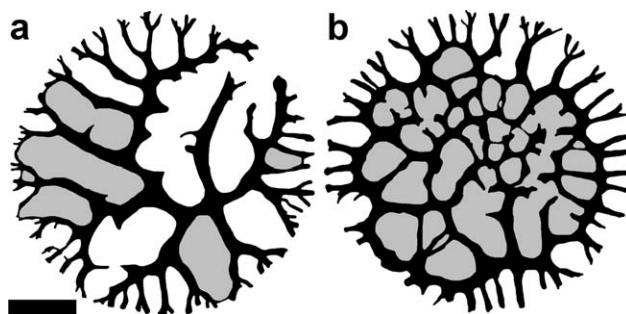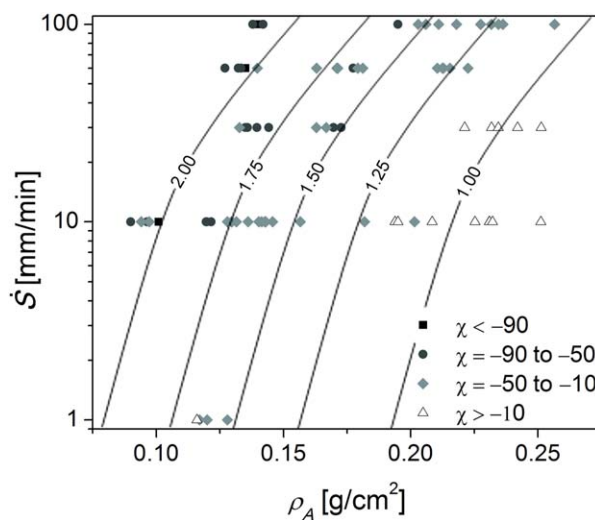

Figure 8. Process map of elongation rate $\dot{S}$ and areal density ρ_A, with all fabricated samples labelled by the corresponding Euler number (χ), and overlaid with contour lines illustrating the trend in N/L. [Color figure can be viewed in the online issue, which is available at wileyonlinelibrary.com.]
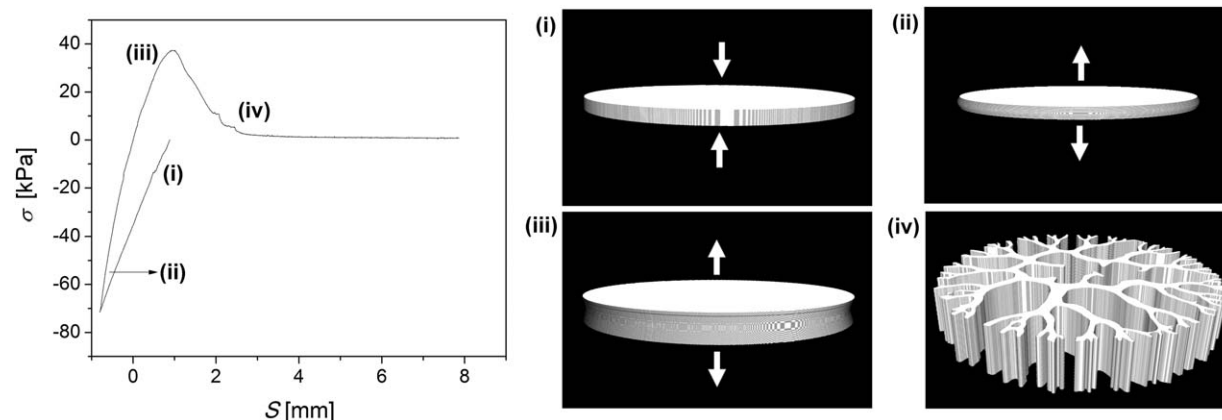
Figure 9. Full fabrication curve (σ, stress, and S, extension) showing all four stages, with compressive stress expressed as negative and tensile stress as positive, with permanent plastic extension beginning at the origin. The locations marked (i–iv) correspond to the images on the right. At the beginning of fabrication, the melt (with thickness t_{cookie}, and diameter d_{blank}) (i) is compressed between Al platens in the furnace. In air, the melt (with t_{melt}, d_f) is stretched uniaxially (ii), and the stress increases to a maximum (iii). At the maximum, air ingress begins as the melt fractures, creating the webs of the stochastic honeycomb (iv). The melt in the webs stretches and some of the webs fracture, creating partial webs and archways until the sample reaches its final height (t_f, d_f) and cools in air.

was compared to the slope of the initial portion of Stage II for the different elongation rates. For $\dot{S} = 1$ mm/min, $\tau_{melt} = 1.7 \pm 0.2$ kPa/s, and for $\dot{S} = 100$ mm/min, $\tau_{melt} = 147 \pm 12$ kPa/s (calculated from the σ-time curve at the onset of melt stretching). Therefore, at the lowest elongation rate, and when $\sigma < 0$ in Stage II, the polymer is experiencing relaxation without any added tensile extension, while at $\dot{S} = 100$ mm/min, the polymer is being extended much faster than the relaxation rate.

At the transition from Stage II to Stage III, the melt morphology changes rapidly as air enters from the perimeter. In rheological studies of the elongation of polymer melts, PP failed through necking.[16–19] However, those studies were done on narrow filaments where the diameter was much smaller than the length, so that $d/l << 1$ (i.e., not flat blanks such as in the present study where $d/l = 6.0–10.0$). A large and quick drop in stress from the peak indicates either rapid ductile necking or cohesive failure.[19,20] A molten filament undergoing cohesive failure would break into two pieces,[20] and ductile failure would result in an elongating neck leading to eventual fracture.[18] In the present case, the melt is neither fracturing across the entire cross section, nor thinning to a point, but undergoes a combi-

nation of the two mechanisms that results in the complex web architecture of stochastic honeycombs. Previous work has shown that the stochastic honeycomb webs are thinner in the central third of the sample,[6] indicating that necking is also occurring during web extension, likely in both the drop in Stage III and the plateau in Stage IV.

Generally, the apparent elongational viscosity, η_E^+, and the strain at failure, ε_B, are reported when referring to the elongational properties of polymer melts.[16,19–26] η_E^+ is calculated[24] through

$$\eta_E^+(t, \dot{\varepsilon}) = \sigma(t, \dot{\varepsilon})\dot{\varepsilon} \qquad (2)$$

where t is time, σ is stress, and $\dot{\varepsilon}$ is the strain rate. Since η_E^+ is a function of time as well as strain rate, it is continuously changing during fabrication; η_E^+ is plotted as a function of time, so the curve exhibits a peak as seen in the σ–extension curves (Figures 9 and 10). $\eta_E^+ - t$ is shown in Figure 13(a) for five samples at the same density and varying $\dot{S}$. At any given time, η_E^+ is larger for samples pulled at a faster $\dot{S}$, as is also seen in rheological melt extension studies.[19,20,25,26] The peaks of the $\eta_E^+ - t$ curves occur at higher η_E^+ as $\dot{S}$ decreases, and η_E^+ at the peak ($\eta_{E,pk}^+$) is plotted as a function of $\dot{\varepsilon}$ in Figure 13(b) for all samples. However, the literature shows that $\eta_{E,pk}^+$ should increase as

Table I. Temperature of the Platens During Melt Elongation at the Beginning and End of each Stage of Fabrication

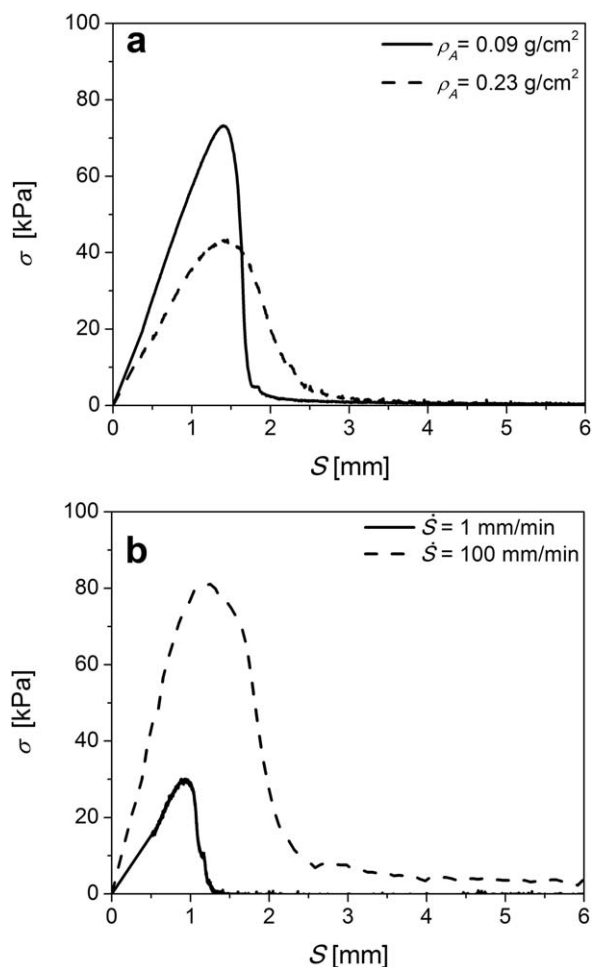| Elongation rate, $\dot{S}$ (mm/min)	Temperature, T (°C)				
	Beginning of stage I	Beginning of stage II	Beginning of stage III	Beginning of stage IV	End of stage IV
1	180	179.3 ± 0.7	165.7 ± 1.8	164.2 ± 0.2	141.0 ± 1.6
10	180	179.6 ± 0.6	178.1 ± 0.4	177.9 ± 0.2	175.9 ± 0.5
30	180	179.3 ± 1.5	178.8 ± 0.3	178.6 ± 0.1	178.0 ± 0.4
60	180	179.4 ± 0.2	178.5 ± 0.2	178.4 ± 0.1	178.1 ± 0.1
100	180	179.0 ± 0.7	178.6 ± 0.2	178.4 ± 0.3	178.1 ± 0.2

Figure 10. Stages II, III, and IV on the fabrication curve for two samples fabricated with the same elongation rate ($\dot{S} = 10$ mm/min) but different densities, $\rho_A = 0.09$ g/cm^2 and 0.23 g/cm^2 (a), and two samples fabricated with the same density ($\rho_A = 0.14$ g/cm^2) and two elongation rates, $\dot{S} = 1$ mm/min and 100 mm/min (b). These curves correspond to the images in Figure 1.
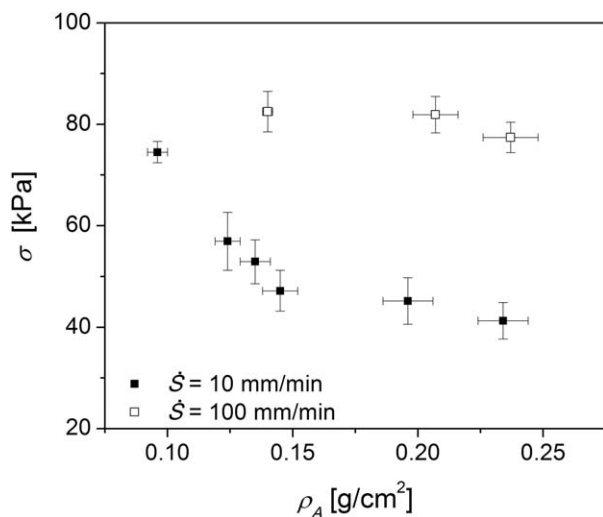
$\dot{\varepsilon}$ increases,[21] which is opposite to the trend observed here. This can be explained by taking the change in temperature into account. From the beginning to the end of Stage II, the temperature of the platens dropped by less than half a degree ($0.4 \pm 0.2°$C) for a melt stretching rate of $\dot{S} = 100$ mm/min, while for $\dot{S} = 1$ mm/min, the temperature dropped by more than ten degrees ($13.6 \pm 1.8°$C) as shown in Table I. The decrease in temperature causes the larger apparent elongation viscosity at low $\dot{\varepsilon}$, as has been shown in the literature.[20]

Contour lines for σ_{pk}, E_{melt}, and $\eta_{E,pk}^{+}$ are overlaid on the process maps in Figure 14, with the data point shapes representing the value of N/L for each sample. The peak PP melt stress and apparent melt stiffness both increase as ρ_A decreases and as $\dot{S}$ increases. Similarly, the apparent melt viscosity at the peak increases as $\dot{S}$ increases, and is also slightly affected by ρ_A. These response parameters are all affected by the molecular structure of the polymer. At the onset of air ingress, structural changes are occurring in the polymer at two distinct length scales. On the molecular scale, polymer chains are shifting and sliding past each other, and stretching between entanglements, while on the
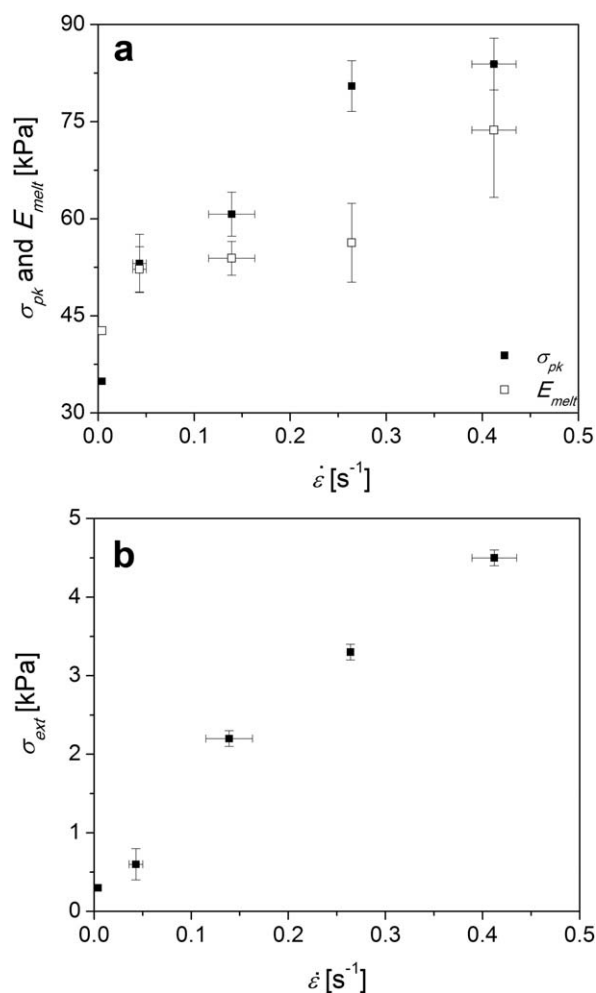

Figure 11. Peak fabrication stress (σ_{pk}) is plotted as a function of areal density (ρ_A) for $\dot{S} = 10$ mm/min and 100 mm/min.

Figure 12. Peak fabrication stress, σ_{pk}, and apparent melt stiffness, E_{melt} (a), and extensional stress, σ_{ext} (b), are plotted as a function of strain rate ($\dot{\varepsilon}$) for samples with $\rho_A = 0.13$ g/cm^2.
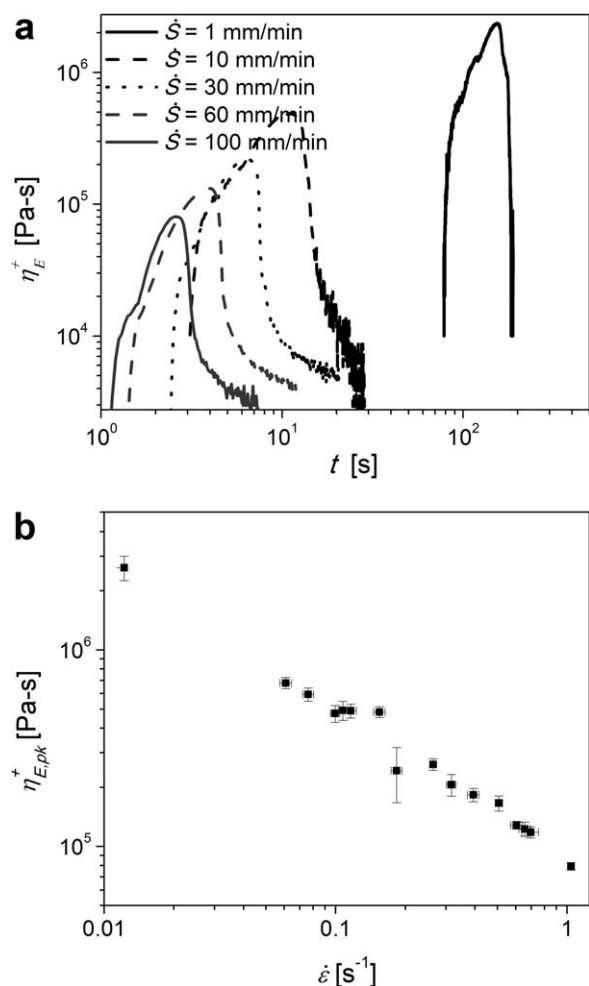
Figure 13. Apparent elongational viscosity, η_E^+, is plotted against time, t, for five samples with $\rho_A = 0.13$ g/cm^2 and increasing elongation rate, $\dot{S}$ (a), and the peak of the elongational viscosity with time, $\eta_{E,pk}^+$, is plotted as a function of strain rate, $\dot{\varepsilon}$, on a log-log scale for all samples.

macroscale, webs are forming and branching, and extending between the skins. Immediately preceding the peak of the fabrication curve, the web must begin to fracture at the outer perimeter, small cracks (cavities) form in the melt and the fine edge structure around the perimeter of the blank is formed (e.g. Figures 3 and 4). In Figure 3(a), with $\dot{S} = 10$ mm/min and $\rho_A = 0.10$ g/cm^2, the fractal area fraction $\lambda = 0.5$, while in Figure 3(e) ($\dot{S} = 10$ mm/min, $\rho_A = 0.23$ g/cm^2), $\lambda = 1$. The low density sample appears to have activated a higher percentage of entanglements on a molecular scale, creating a larger number of nodes than the high density sample. Figure 4(a) ($\dot{S} = 1$ mm/min, $\rho_A = 0.13$ g/cm^2) has $\lambda = 0.7$, while Figure 4(e) ($\dot{S} = 100$ mm/min, $\rho_A = 0.13$ g/cm^2) has $\lambda = 0.3$. Here, as $\dot{S}$ increases, more entanglements are activated and the average number of nodes in the architecture increases from 245 [Figure 4(a)] to 440 [Figure 4(e)]. Figure 3(a) and Figure 4(e) have $\sigma_{pk} > 70$ kPa, while Figures 3(e) and 4(a) have $\sigma_{pk} \approx 40$ kPa. This higher σ_{pk} could indicate the higher stress required to deform the polymer to allow a path for air into the centre of the sample.
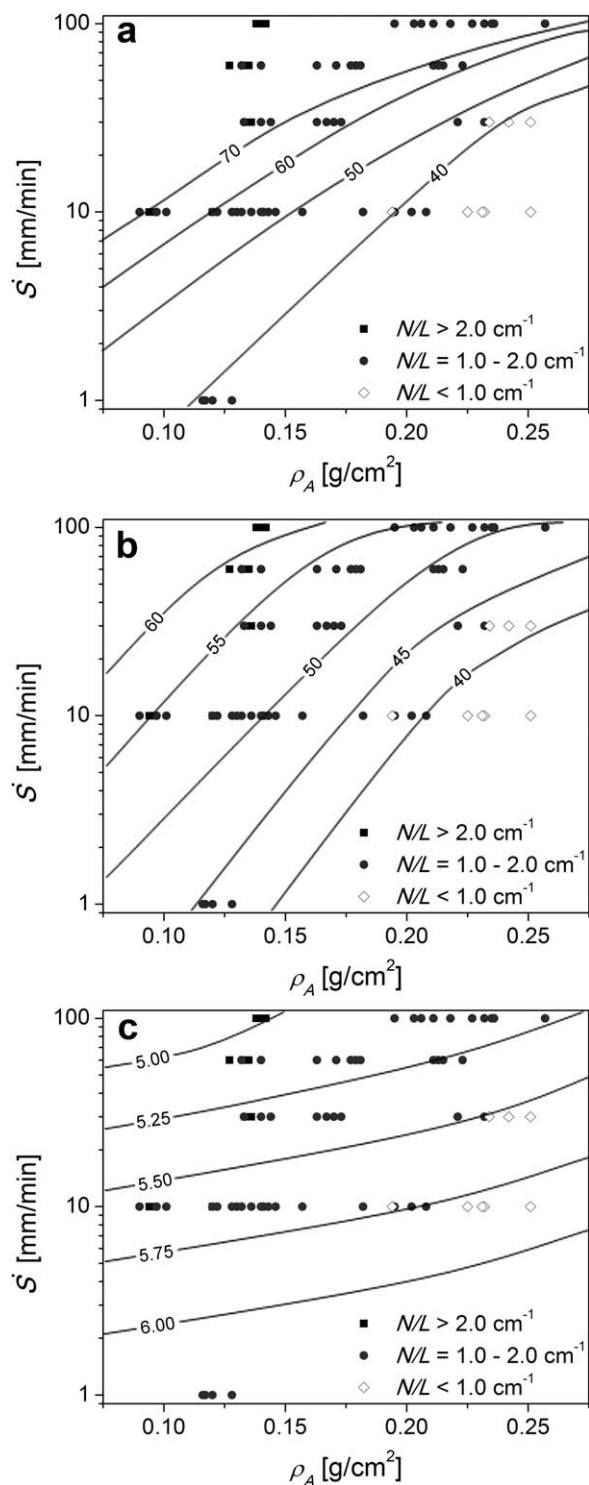

Figure 14. The process map plotting elongation rate, $\dot{S}$, against areal density, ρ_A, showing the samples fabricated, with variation in N/L shown in the data points. Contour lines illustrating the trends in σ_{pk} (a), E_{melt} (b) and $\log \eta_{E,pk}^+$ (c) are superimposed on top.

CONCLUSION

The melt-stretching of PP stochastic honeycombs was studied in detail and subdivided into four stages based on the mechanical response of the polymer melt. At the peak stress, cavitation

created air pockets that then propagated as cracks towards the centre of the structure. The low melt stretching rates were found to be on the same order of magnitude as the apparent relaxation rate of the PP, while at higher melt stretching rates the PP was being extended much more quickly than the polymer chains could realign. Lower melt stretch rates and higher density both led to lower peak stress (σ_{pk}) and stiffness (E_{melt}) during melt stretching, as well as higher apparent elongation viscosity ($\eta_{E,pk}^{+}$). The melt stretch rate played an important role in determining the architecture of the webs. A slower rate gave a less negative Euler number, χ, while a faster rate exceeded the ability of the polymer chains to reorient, creating a structure with more apparent (projected) closed cells (smaller λ, and more negative χ). At lower melt stretch rates, density also played a significant role in the architecture, with a smaller number of nodes per length of webs, N/L, at higher density. These results illustrate that it will be possible to tune the final architecture by varying the fabrication conditions.

REFERENCES

1. Gibson, L. J.; Ashby, M. F. Cellular Solids: Structures and Properties, 2 ed.; Cambridge University Press: Cambridge, NY, **1997**.

2. Karlsson, K. F.; Åström, T. B., *Compos. A* **1997**, *28*, 97.

3. Gendron, R., ed. Thermoplastic Foam Processing: Principles and Applications. CRC Press: Boca Raton, FL, **2005**.

4. Hostetter, M.; Cordner, B.; Hibbard, G. D. *Compos. B* **2012**, *43*, 1024.

5. Hostetter, M.; Hibbard, G. D. *J. Mater. Sci.* **2014**, *49*, 8365.

6. Hostetter, M.; Hibbard, G. D. *J. Appl. Polym. Sci.* **2014**, *131*, 40074.

7. ASTM D1238 - 13 Standard Test Method for Melt Flow Rates of Thermoplastics by Extrusion Plastometer. ASTM International: West Conshohocken, PA, 2014; Vol. D1328.

8. Schröder-Turk, G. E.; Mickel, W.; Kapfer, S. C.; Klatt, M. A.; Schaller, F. M.; Hoffmann, M. J. F.; Kleppmann, N.; Armstrong, P.; Inayat, A.; Hug, D.; Reichelsdorfer, M.; Peukert, W.; Schwieger, W.; Mechke, K., *Adv. Mater.* **2011**, *23*, 2535.

9. Ohser, J.; Muücklich, F. Statistical Analysis of Microstructures in Materials Science. Wiley: Chichester, West Sussex, England, **2000**; p 375.

10. Michielsen, K.; De Raedt, H., *Phys. Rep.* **2001**, *347*, 461.

11. Fried, J. R., Polymer Science and Technology. 2nd ed.; Prentice Hall PTR: Upper Saddle River, NJ, **2003**.

12. Zhou, Y.; Mallick, P. K. *Polym. Eng. Sci.* **2002**, *42*, 2449.

13. Münstedt, H. *J. Rheol.* **1980**, *24*, 847.

14. Laun, H. M. *J. Rheol.* **1986**, *30*, 459.

15. Laun, H. M.; Münstedt, H. *Rheol. Acta* **1978**, *17*, 415.

16. Malkin, A. Y.; Petrie, C. J. S. *J. Rheol.* **1997**, *41*, 1.

17. White, J. L.; Ide, Y. *J. Appl. Polym. Sci.* **1978**, *22*, 3057.

18. Ide, Y.; White, J. L. *J. Non-Newtonian Fluid Mech.* **1977**, *2*, 281.

19. Ide, Y.; White, J. L. *J. Appl. Polym. Sci.* **1978**, *22*, 1061.

20. Lee, J.; Solovyov, S. E.; Virkler, T. L.; Scott, C. E. *Rheol. Acta* **2002**, *41*, 567.

21. Dealy, J. M.; Larson, R. G. Structure and Rheology of Molten Polymers: From Structure to Flow Behavior and Back Again. Hanser Gardner Publications: Cincinnati, OH, **2006**.

22. Considère, A. *Annales des Ponts et Chaussées* **1885**, *9*, 574.

23. McKinley, G. H.; Hassager, O. *J. Rheol.* **1999**, *43*, 1195.

24. Su, F. H.; Yan, J. H.; Huang, H. X. *J. Appl. Polym. Sci.* **2011**, *119*, 1230.

25. Lagendijk, R. P.; Hogt, A. H.; Buijtenhuijs, A.; Gotsis, A. D. *Polymer* **2001**, *42*, 10035.

26. Minoshima, W.; White, J. L.; Spruiell, J. E. *Polym. Eng. Sci.* **1980**, *20*, 1166.